ADVANCED MATERIALS

Supporting Information

for *Adv. Mater.*, DOI: 10.1002/adma.201707196

3D Jet Writing: Functional Microtissues Based on Tessellated Scaffold Architectures

*Jacob H. Jordahl, Luis Solorio, Hongli Sun, Stacy Ramcharan, Clark B. Teeple, Henry R. Haley, Kyung Jin Lee, Thomas W. Eyster, Gary D. Luker, Paul H. Krebsbach, and Joerg Lahann**

Supporting Information

3D Jet Writing: Functional microtissues based on tessellated scaffold architectures

*Jacob H. Jordahl, Luis Solorio, Hongli Sun, Stacy Ramcharan, Clark B. Teeple, Henry R. Haley, Kyung Jin Lee, Thomas W. Eyster, Gary D. Luker, Paul H. Krebsbach, Joerg Lahann**

1. Supplementary Methods

1.1 Fiber straightness analysis

A series of linear stage movements in the x-direction were performed to create a horizontal array of electrospun fibers. The speed increased by 3 mm/s for each fiber row. As the speed increased, the liquid-coil effect was decreased until at a critical speed it was eliminated entirely. To examine how straight the depositing fiber was, the second fiber after elimination of the liquid-coil effect was chosen for analysis both with and without an electrostatic lens using the same polymer solution. Photographs of the horizontal array of fibers were taken on a Canon EOS 20D DSLR camera, and the fiber in question was examined using MATLAB. The top and bottom edge of the fiber were found using a custom MATLAB code. The middle of the fiber was determined by taking the value midway between the top and bottom edge. This was done across the entire image to obtain a scatterplot representing the fiber in the photograph. A five-point running average was used to smooth the data. Linear regression of the scatterplot data provided a perfectly straight line, and the root mean square error was calculated for a total of seven samples for the samples with and without the secondary ring electrode. The root mean square error provided an estimate for how far the fiber deviated from a perfectly straight line on average. The average root mean squared error is reported as the straightness from centerline. With a ring present this value was 0.6 pixel deviation from the regression line, which is potentially artificially high due to the data being within the noise levels of the analysis. With no ring present, the deviation from the regression line was 2.3 pixels, indicating nearly a fourfold increase in straightness when an electrostatic lens is implemented. (Table S1).

1.2 Scaffold Characterization

Scaffold porosity calculated by taking the ratio of the void volume within the scaffold to the total volume. Fluorescent images were taken on a Nikon A-1 inverted confocal laser scanning microscope (CLSM), and were processed on Imaris (Version 7.5) software. Scanning electron micrographs were obtained from an AMRAY 1910 Field Emission Scanning Electron Microscope (FEG-SEM). Photographs of resulting structures were taken with a Canon EOS 20D Digital Single-Lens Reflex (DSLR) camera.

1.3 ImageJ analysis

Values for parallelism, perpendicularity, and geometric consistency were determined by using ImageJ software. Parallelism was determined by manually measuring the angle at which the fiber stacks were deposited. The average root mean square error (RMSE) of the measured angle to the average was reported as the ‘parallelism’ of the fibers (n= 82). Perpendicularity was determined by a similar method in ImageJ. Angles of the fibers at each intersection were measured. The RMSE of difference between the angles and 90° was reported as the ‘perpendicularity’(n= 560). Geometric consistency was the third value determined using ImageJ analysis (n= 70). The distance between parallel rows and columns of fiber stacks was

measured across three entire scaffolds to determine the consistency between the fiber stack spacing. The RMSE was calculated from the difference between the measured fiber stack spacing and the average spacing across all the fiber stacks. The average RMSE was divided by the average fiber stack spacing to yield the percentage reported as the geometric consistency. All measurements were taken across three entire scaffolds consisting of 500 μm square pores.

2. Supplementary Text

2.1 3D jet writing

Polymer solutions are pumped through parallel capillaries which are electrified using positive DC high voltage power supplies. Under an electric field, the solution forms a fluid jet which traverses through the ring secondary electrode. The ultra-stable jet solidifies into a polymer fiber as it deposits onto a collection electrode mounted on two positioning stages arranged for x-y motion.

The relationship between the electric field and electric potential can be translated into stabilizing forces provided by the ring secondary electrode through the following equation:

$$\vec{E} = \vec{F} / q = -\vec{\nabla} V \tag{1}$$

where $\vec{E}$ is the electric field, $\vec{F}$ is the electrostatic force, q is charge, and V is electric potential. The direction of the electric field is defined as the direction of the force on a positive unit charge.

2.2 Secondary ring electrode design

One factor which contributes to the overall focusing capability of the secondary ring electrode was the positioning of the bottom of the ring relative to the grounded collection electrode. While increases in focusing capability was seen by increasing the ring height, similar increases in focusing were found by simply lowering a ring of lesser height such that it was a similar distance from the grounded electrode (Figure S1 – S4). However, differences were observed in the driving force on the depositing fiber jet in the two cases. The ring with greater height had an increased driving force than the shorter ring electrode, indicating that maximizing ring height was a superior method of increasing focusing compared to moving a smaller ring closer to the grounded electrode (Figure S5). However, changing ring height while maintaining the z-position of the center of mass leads to the same minimum driving force, with enhanced focusing seen from the rings of greater height (Figure S6).

Changing the applied electric potential on the charged capillary yielded a couple interesting findings. First, it was seen that this does not have any significant effect on the focusing provided by the secondary ring electrode (Figure S7). The plots of the electric potential energy wells and the radial component of the electric field all overlap with one another, indicating that there is no distinguishing difference in the focusing capability within the range of applied electric potentials examined (from 14 kV to 20 kV). However, what did change with increasing applied potential was the driving force. As the applied potential was increased, the driving force acting on the depositing fiber jet also increased. This caused the minimum driving force to transition from negative at 14 kV, around zero at 16 kV, to positive values for higher applied potentials. This method of altering the 3D jet writing environment provides a means for controlling the deposition speed of the fiber jet without affecting the focusing ability of the secondary ring electrode. A larger driving force acting on the

depositing fiber jet will result in more acceleration, and higher jet velocities upon deposition on the grounded collection electrode.

If the applied electric potential to the secondary ring electrode were altered, changes in both the focusing and driving forces are seen to change (Figure S8). As would be expected, increases in the applied electric potential leads to an increased focusing force produced by the electrode. This can be explained by the increased charge density on the copper ring electrode which results in an increased radial component of the electric field. As the applied electric potential increases, the driving force decreases, and at sufficiently high applied potentials can even become negative. Physically, this can be used to determine how the ring affects the depositing fiber jet for a given fixed secondary ring electrode geometry. Increasing the applied potential to the ring electrode results in increased focusing, but can also be used to decrease the driving force applied to the jet. This is important as it is a means of adjusting the driving force acting on the depositing fiber jet without altering the amount of charge being input into the polymer solution being electrospun. Using the combination of both changing the capillary and secondary ring electrode applied potentials can be used independently to tune the depositing jet speed and the focusing capabilities of the system.

Altering the diameter of the secondary ring electrode also leads to changes in the resultant radial electric field and driving force pulling the fiber towards the grounded collection electrode. It was seen that ring electrodes with smaller diameters yielded a stronger focusing capability, even though the larger diameter ring electrodes produced deeper electric potential energy wells (Figure S9). However, the driving force which accelerates the polymer fiber to the grounded electrode is also a characteristic of importance. Modeling the electric potential along the z axis (with x,y=0) for secondary ring electrodes of varying diameter allows us visualize the driving force on the depositing polymer fiber. This will be utilized to predict which ring configuration will minimize this uneven fiber deposition. Simulations indicated that smaller diameter secondary electrodes have locations near the middle of the ring where the driving force nearly goes to zero (Figure S10). However, as the secondary ring electrode diameter increases, the driving force gets larger. Therefore, there is a tradeoff between having enhanced focusing provided by the ring, and the ability of the ring to provide even fiber deposition.

2.3 Fiber patterning

After defining the desired electric fields in the electrospinning setup, the effect of the secondary ring electrode was tested by depositing electrospun PLGA fibers on grounded collection electrode which was mounted to a dual axis motion control unit. This provided the means for depositing the fibers in controlled patterns by programming the x-y stage movements. Upon achieving a stable fluid jet, setting the collector speed to match that of the depositing polymer jet is critical to creating straight fiber deposition (Figure S11). When the collection speed is too slow, the liquid rope-coil effect is observed, leading to buckling and coiling of the depositing fiber jet, as seen in Supplemental Movie 1. Initial testing was performed by simply testing one-dimensional movement to determine what effect the ring electrode has on focusing the fiber deposition. The stage was programmed to create an array of horizontal lines spaced 3 mm apart. At the start of each new horizontal segment the stage speed was increased by a factor of 3 mm/s until the stage reached 48 mm/s. A representative resulting fiber deposition pattern is depicted in Figure S12 with both with (Top) and without (Bottom) a secondary ring electrode.

Fabrication of scaffolds is generally performed through the organization of straight lines to create a desired scaffold pattern. However, simply drawing arbitrary straight line segments often does not result in organized fiber structures. Due to the nature of the depositing fiber, the grounded collection substrate is moved at a speed slightly greater than the depositing fiber jet. When creating fiber scaffolds, changes in direction are made outside of the desired

scaffold area to ensure consistent fiber deposition. These changes in direction also include a zone in which the depositing fiber is allowed to catch up to the collection electrode (Figure S13). This is accomplished by incorporating a 'slow speed' segment in the programmed stage movement. When the fiber jet catches up to the stage movement, fiber coils are deposited until it reaches the next straight fiber segment, at which point the stage accelerates back to the 'fast speed'. These elements are critical for the design of organized fiber structures.

In addition to the changes in collection electrode speeds, a 'lead in length'(indicated by L in Figure S14) is often desired. These are simply lengths of unused fibers which come before or after the desired scaffold architecture. The purpose of these lead in lengths is to: 1) allow the stage to accelerate to the proper deposition speed, 2) allow the fiber time to settle into the desired deposition location, and 3) ensure the fiber is deposited across the entire desired scaffold area prior to changing directions. This lead in length can be independently changed without altering the final scaffold architecture, and should be optimized to maximize deposition precision and minimize wasted material and fabrication time. Other parameters which are used in scaffold design include the pore size (p), the number of fiber stacks (s), and the number of pores (n) within a square scaffold structure. These values are illustrated in Figure S14.

2.4 Controlling fiber deposition

Controlling the speed of the depositing fiber was achieved by modulating the applied electric potential to either the ring or the needle. Typical writing speeds ranged from 20 mm/s to 40 mm/s, with maximum speeds reaching in excess of 100 mm/s (Figure S15). The jet writing system is sensitive to external stimuli, including environmental factors. It was found that humidity is one environmental parameter that has an impact on stability. 27% – 35% relative humidity at 27°C was found to be the optimal operating condition. User defined, customizable 3D constructs can be fabricated using 3D jet writing. Patterns are designed in CAD and converted to stage movements through LabView.

With the ability to control the deposition of straight fiber segments, organized arrays of fibers relative to one another are used to create complex 3D structures. Upon initial jet formation, a stabilization time is often necessary where the fiber speed changes, typically the jet will start depositing very slow and gradually speed up to normal deposition speeds near 30 mm/s. Deposition speed can be controlled during the jetting process through the alteration of the jetting parameters, namely the applied electric potential to the ring and the needles. Other parameters which affect the deposition of the fibers include the ring/needle height, ring electrode dimensions, solution flow rate, solution composition, and environmental conditions such as humidity and temperature. The fiber deposition speed is determined prior to any programmed stage movements simply by moving the collection electrode back and forth at increasing the speed until a lag in the depositing fiber jet is seen. Stabilization of the fiber jet is confirmed by continuing to move the collection electrode at this speed. If the lag in the fiber deposition is consistent, the jet is considered stabilized.

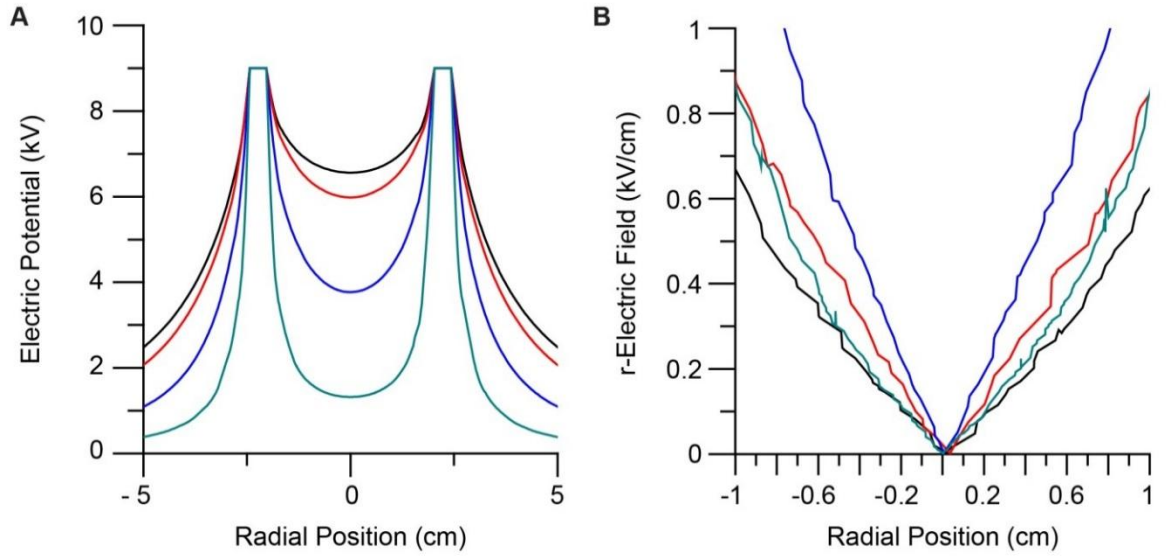

Figure S1. Finite element simulations of the electrostatic potential for various ring electrodes heights in 3D jet writing experiments. A) The electric potential of 3D jet writing experimental setup, which includes a ring shaped secondary electrode. Simulations are taken at the bottom of rings 1 cm, 2 cm, 3 cm, and 3.5 cm in height each 1 cm below the tip of the charged capillary (black, red, blue, and green respectively). B) The slope of the electric potential plots from (A) are plotted to visualize the radial component of the electric field, representing the focusing capability of each ring type.

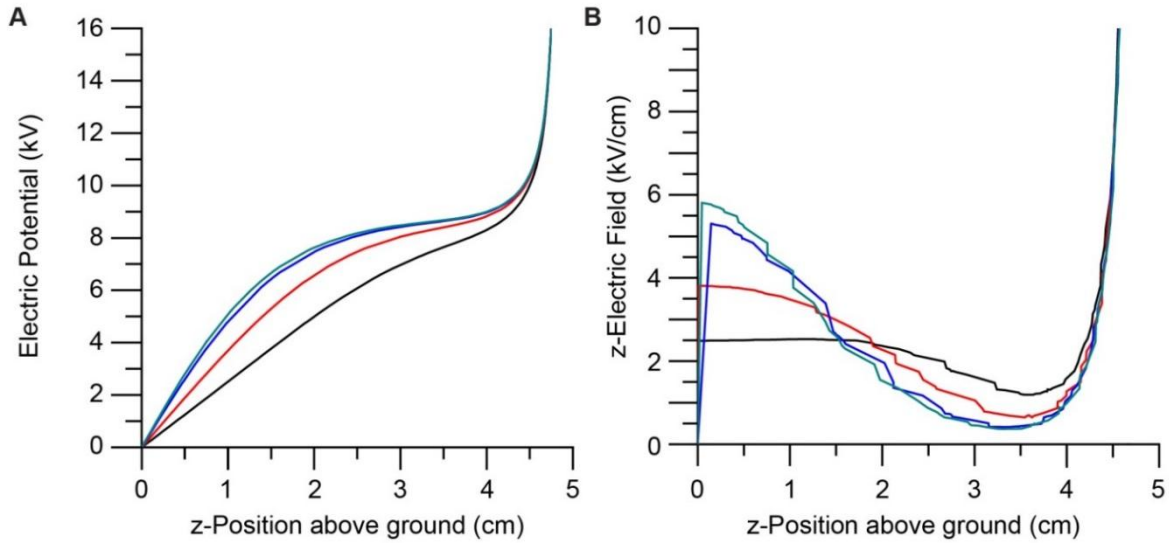

Figure S2. Finite element simulations which represent how the driving force changes with changing ring electrode height. A) The electric potential along the z-axis of 3D jet writing experimental setup. Simulations are taken at the bottom of rings 1 cm, 2 cm, 3 cm, and 3.5 cm in height each 1 cm below the tip of the charged capillary (black, red, blue, and green respectively). B) The gradient of the plots in (A) show the 'driving force' which is the z-component of the electric field. Lower values of electric field represent a loss in driving force.

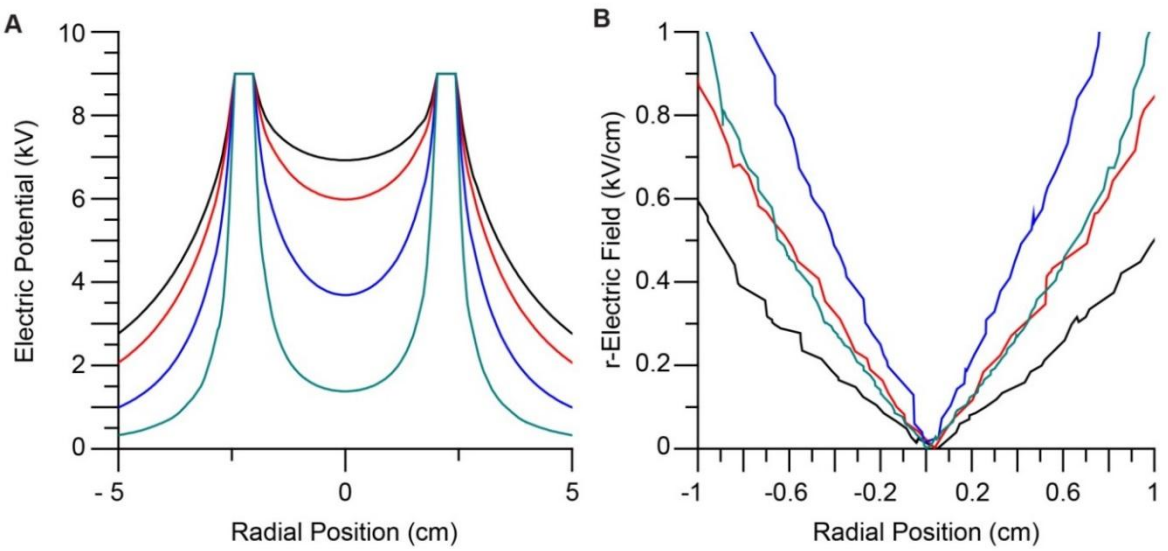

Figure S3. Finite element simulations of the electrostatic potential for various ring electrode positions in 3D jet writing experiments. A) The electric potential of 3D jet writing experimental setup, which includes a ring shaped secondary electrode. Simulations are taken at the bottom of rings positioned 0 cm, 1 cm, 2 cm, and 2.5 cm below the tip of the charged capillary (black, red, blue, and green respectively). B) The slope of the electric potential plots from (A) are plotted to visualize the radial component of the electric field, representing the focusing capability of each ring type.

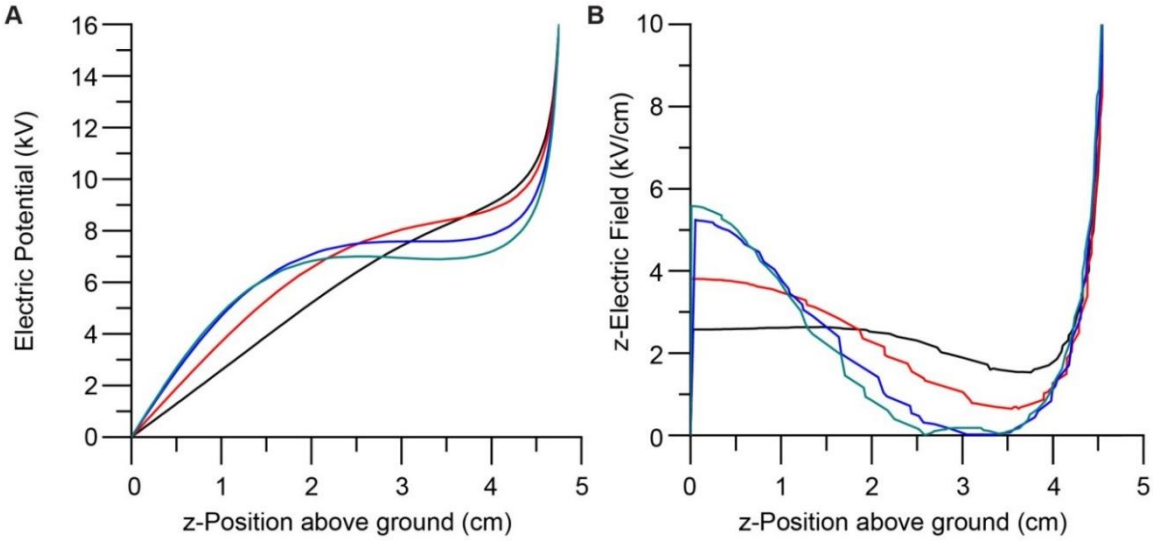

Figure S4. Finite element simulations which represent how the driving force changes with changing ring electrode z position. A) The electric potential along the z-axis of 3D jet writing experimental setup. Simulations are taken at the bottom of rings positioned 0 cm, 1 cm, 2 cm, and 2.5 cm below the tip of the charged capillary (black, red, blue, and green respectively). B) The gradient of the plots in (A) show the 'driving force' which is the z-component of the electric field. Lower values of electric field represent a loss in driving force.

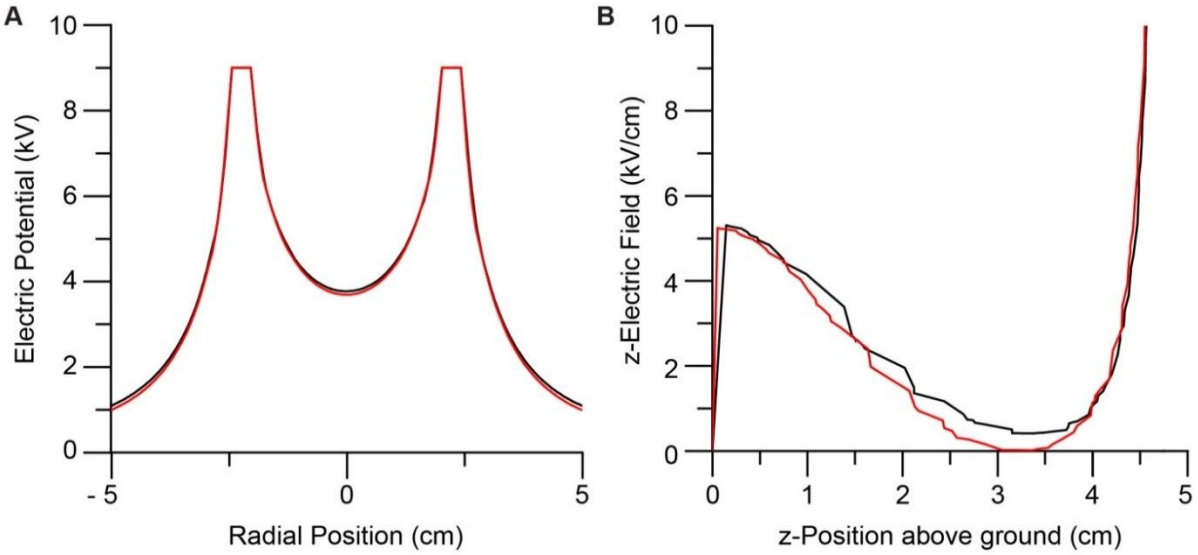

Figure S5. Comparing effect of changing the ring height and moving the ring electrode. A) Overlay of the electric potential wells produced by two different secondary ring electrodes. The red line indicates a ring electrode 2 cm in height 2 cm below the capillary tip. The black line represents a 3 cm ring electrode 1 cm below the capillary tip, placing the bottom of the ring in the same location in each case. Similar focusing capability is observed for each electrode configuration. B) Looking at the driving force produced by the z-component of the electric field shows that the 3 cm ring electrode has more driving force than the shorter ring electrode.

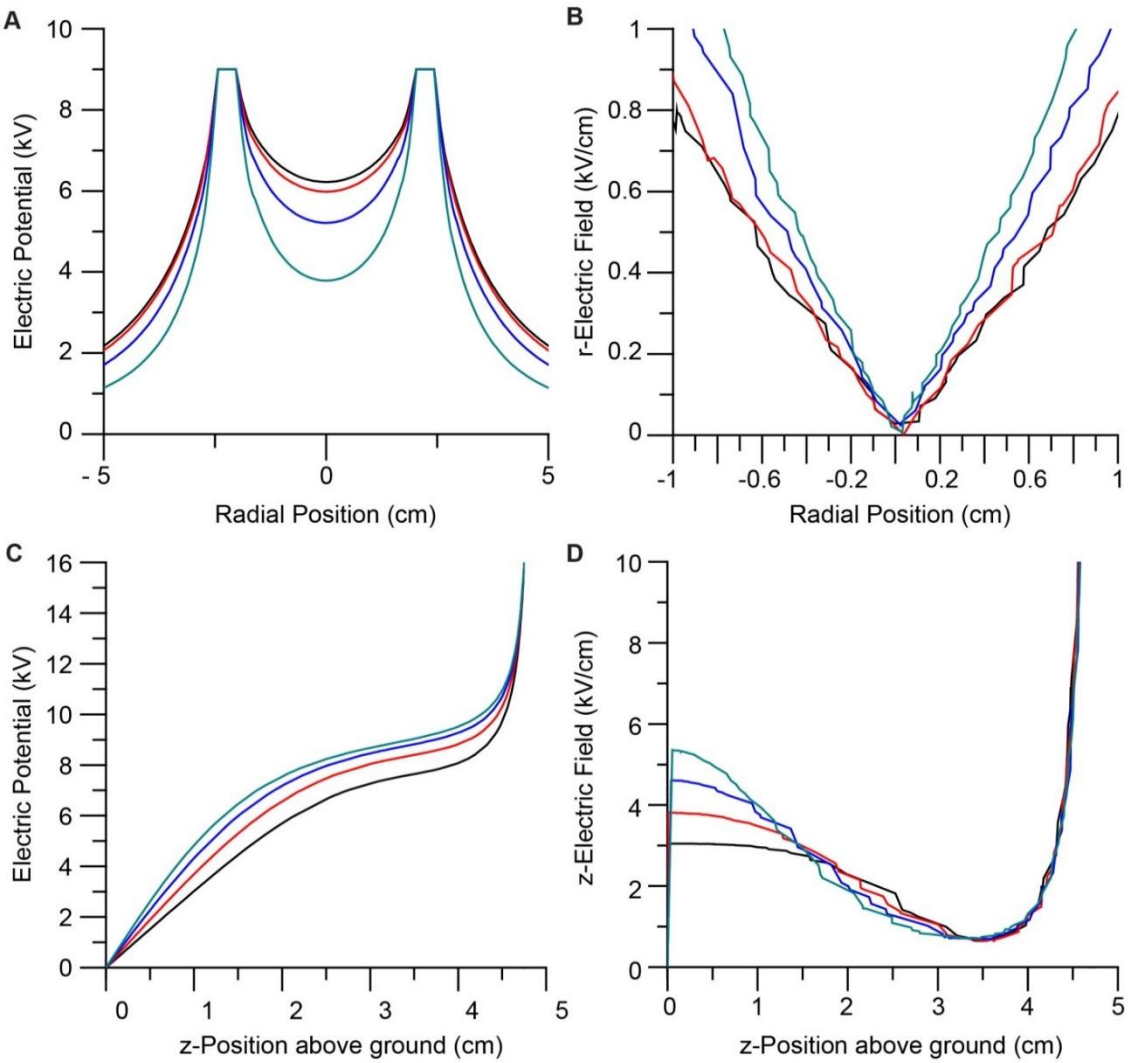

Figure S6. Effect of changing the ring height while maintaining the center of mass. A) The effect of four secondary ring electrode configurations was examined. Electric potential wells of 1 cm, 2 cm, 3 cm, and 4 cm (black, red, blue, and green respectively) in height show changes in the depth of the wells and B) focusing seen from simply moving the ring closer to the collection electrode. C) Plotting how the electric potential along the z-axis changes with ring height and maintained center of mass, shows a similar profile for each case. D) The slope of the plots from (C) show the z-component of the electric field which contributes to the driving force. This shows each ring has the same minimum driving force.

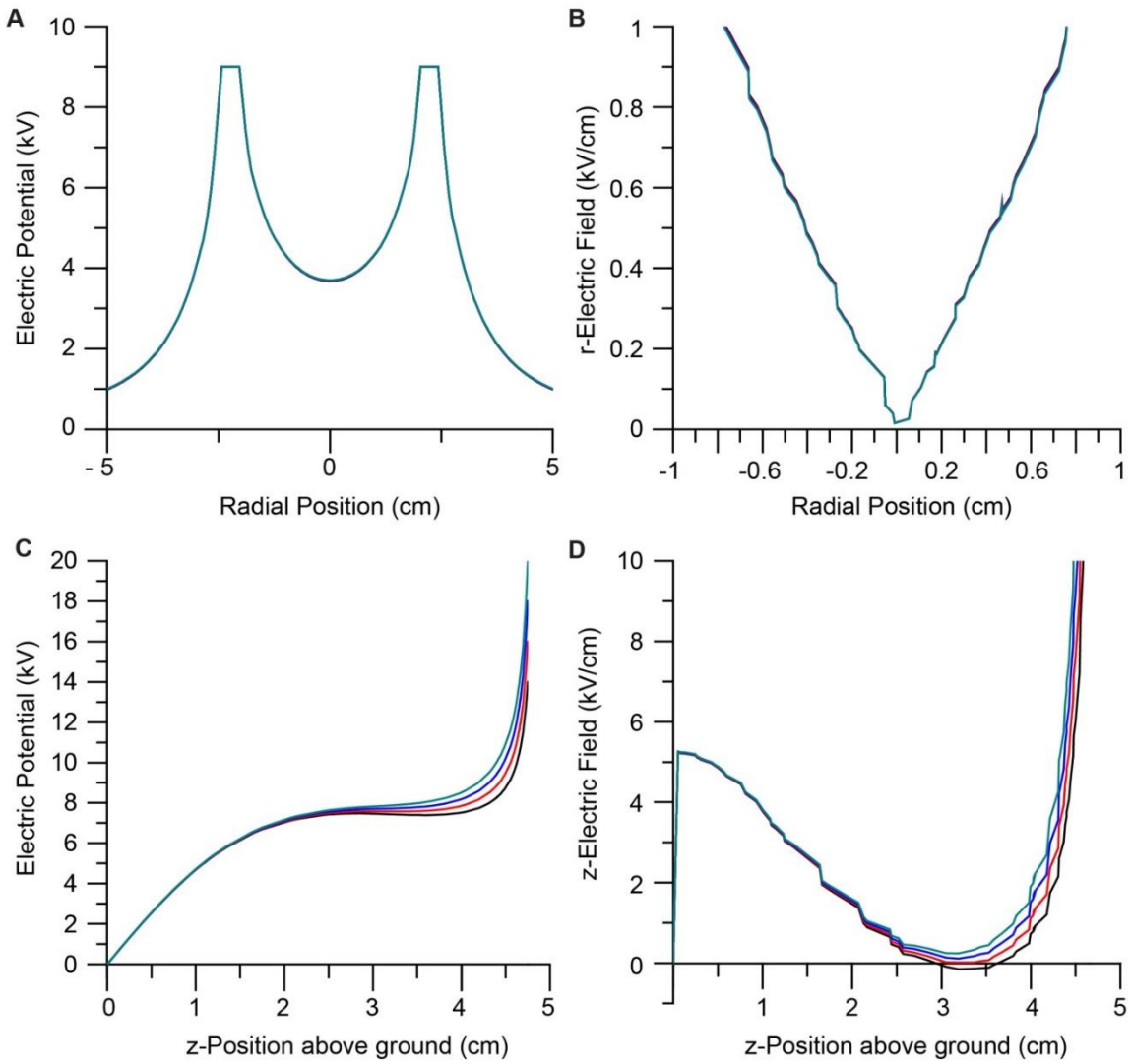

Figure S7. Determination of how changing the electric potential applied to charged capillary affects focusing and driving forces in 3D jet writing. A-B) Radial components of the electric potential (A) and electric field (B) were examined for varying applied DC electric potential to a charged capillary with a constant applied potential to the secondary ring electrode of 9 kV. Simulations of applied voltages of 14 kV, 16 kV, 18 kV, and 20 kV (black, red, blue, and green respectively) to the capillary tip demonstrate minimal effects on focusing. All lines overlap with each other, giving the perspective that there is only one plot in these examples. C-D) Z-components of the electric potential (C) and electric field (D) demonstrate that the applied electric potential does play a role in affecting the driving force acting on the depositing fiber jet. At lower applied potentials (14 kV), negative driving force can be seen, with continual increases with increasing applied potential.

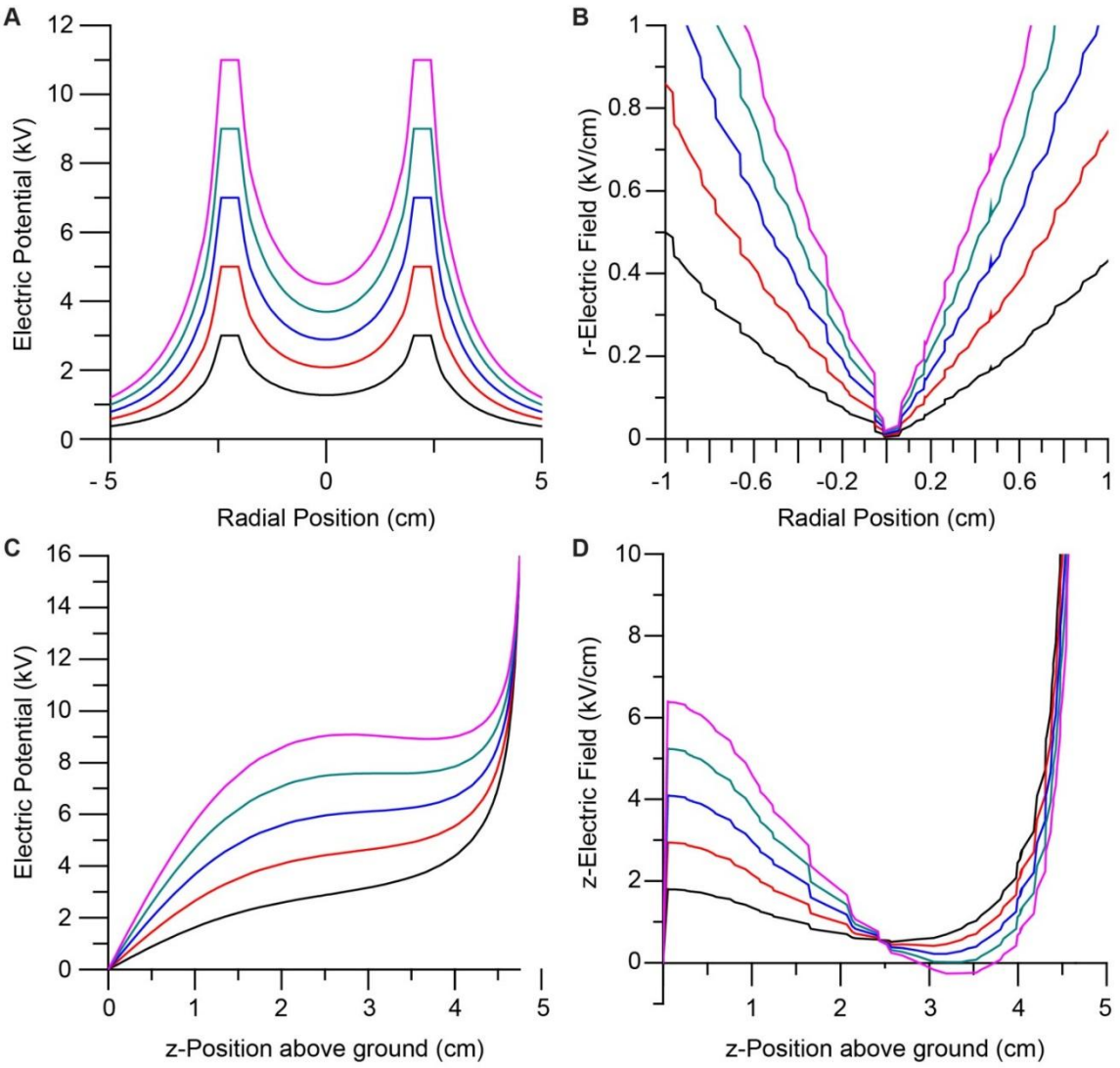

Figure S8. Determination of how changing the electric potential applied to secondary ring electrode affects focusing and driving forces in 3D jet writing. A-B) Radial components of the electric potential (A) and electric field (B) were examined for varying applied DC electric potential to the secondary ring electrode with a constant applied potential to the charged metal capilary of 16 kV. Simulations of applied voltages of 3 kV, 5 kV, 7 kV, 9kV, and 11 kV (black, red, blue, green, and pink respectively) to the capillary tip demonstrate consistent increases in focusing with increasing ring potential. C-D) Z-components of the electric potential (C) and electric field (D) demonstrate that the applied electric potential does play a role in affecting the driving force acting on the depositing fiber jet. As expected, increasing applied potential decreases the driving force on the depositing fiber jet. This emphasizes the importance of how the ring potential can be used to control the speed and focusing in the 3D jet writing system.

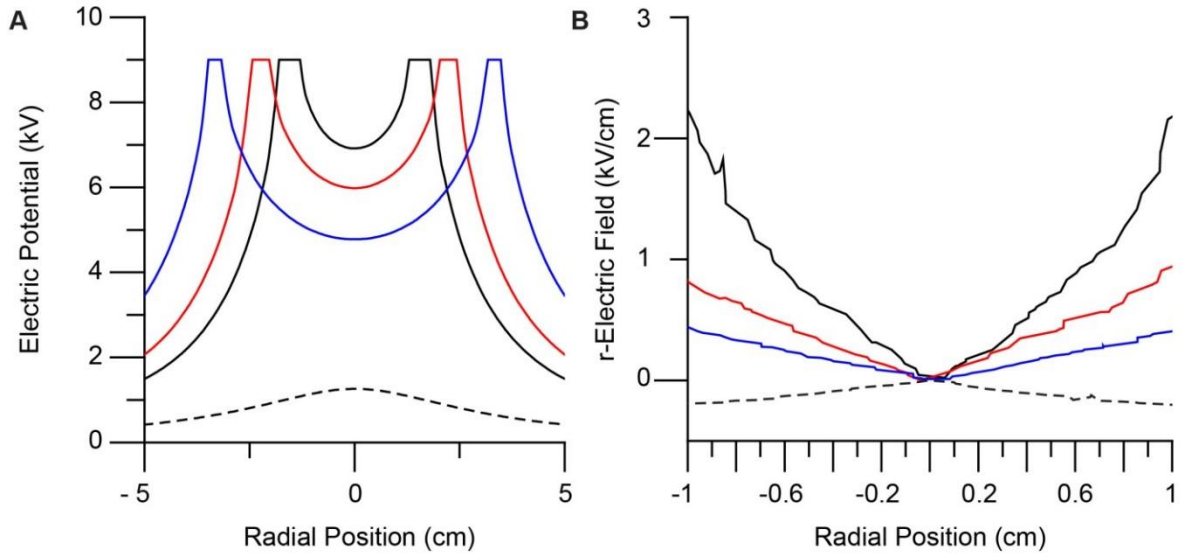

Figure S9. Finite element simulations of the electrostatic potential for various diameter ring electrodes in 3D jet writing experiments. A) The electric potential of 3D jet writing experimental setup, which includes a ring shaped secondary electrode. Simulations for rings of 1inch, 1.5 inch, and 2.5 inches in diameter are shown at a distance 3 cm below the charged capillary tip (black, red, and blue respectively). The dashed black line indicates the electric potential without a ring electrode. B) The slope of the electric potential plots from (A) are plotted to demonstrate the focusing capability of each ring type. The 1 inch ring has higher electric fields (i.e. more focusing) compared to the other rings, and all rings are opposite in sign from the configuration without a ring electrode.

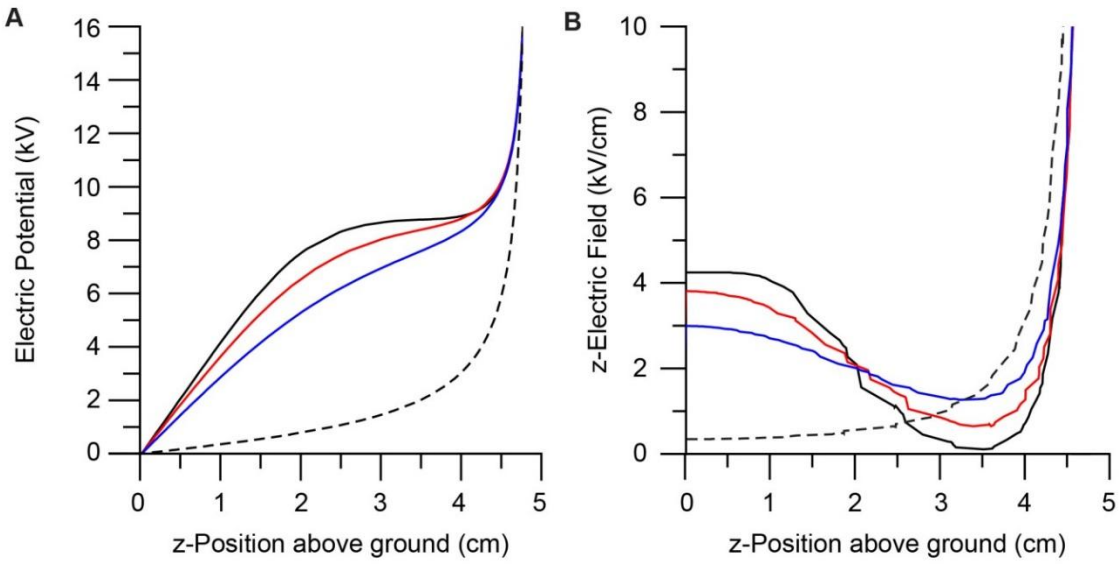

Figure S10. Finite element simulations which represent how the driving force changes with changing ring electrode diameter. A) The electric potential along the z-axis of 3D jet writing experimental setup, which includes a ring shaped secondary electrode. Simulations for rings of 1inch, 1.5 inch, and 2.5 inches in diameter are shown at the bottom of the ring electrode (black, red, and blue respectively). The dashed black line indicates the electric potential without a ring electrode. B) The gradient of the plots in (A) show the 'driving force' which is the z-component of the electric field. This field is responsible for accelerating the jet towards the grounded collection electrode. Lower values of electric field represent a loss in driving force.

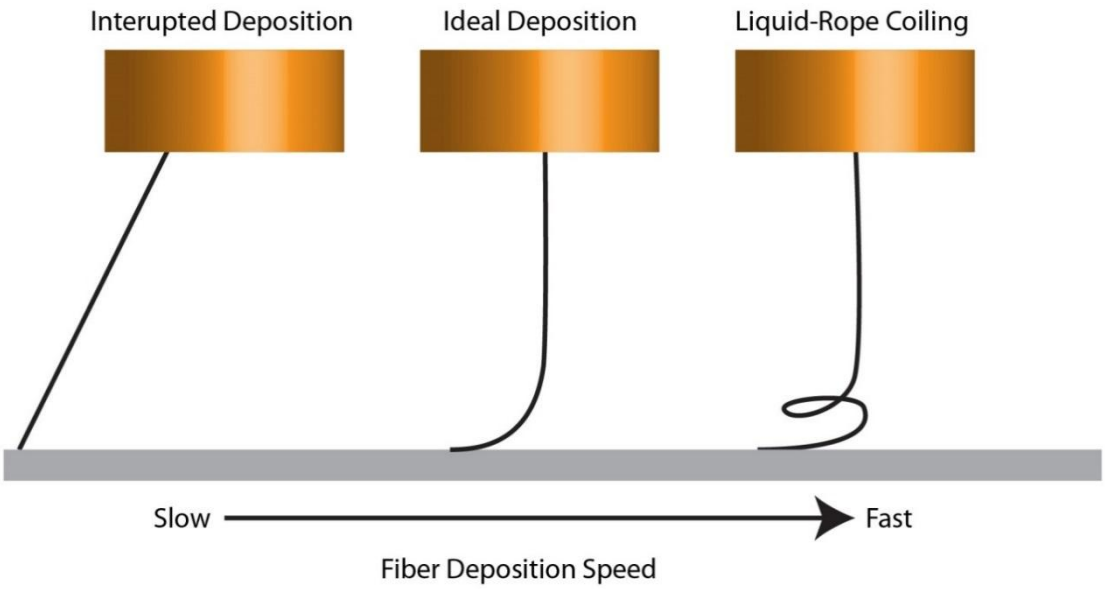

Figure S11. Fiber deposition regimes. The three major fiber deposition regimes exist. Ideal fiber deposition occurs when the fiber deposition speed is slightly slower than the collection electrode. This type of deposition is characterized by visible lag in the depositing jet. If the depositing fiber jet is faster than the speed of the collection electrode, a liquid-rope coiling effect arises. This type of deposition results in fibers deposited in rings or oscillatory structures. Finally, interrupted deposition occurs when the fiber deposition is either very slow or intermittent. This results in poor fiber organization and indicates a change in jetting conditions is necessary.

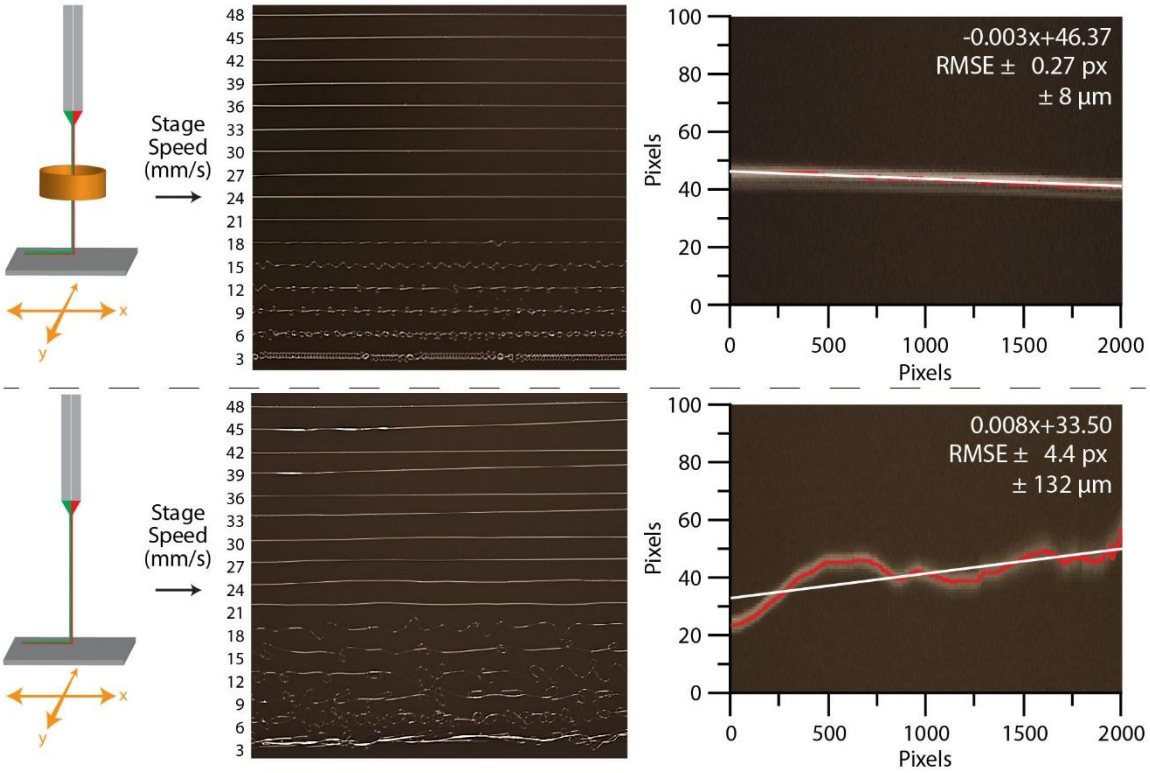

Figure S12. Implementation of a ring secondary electrode enhances precision of fiber deposition. Polymer fibers were deposited in an increasing range of collection speeds. Once the stage reaches a speed greater than the speed of the depositing jet (24 mm/s), buckling and coiling is eliminated, leading to straight fiber segments. These segments were analyzed both with (top), and without (bottom), ring secondary electrode. Analysis of the resultant fibers in Matlab demonstrate that the fibers deposited with a stabilizing ring electrode are within 8 µm of a perfectly straight line, whereas without the stabilizing ring the fiber is within 123 µm. This ability to create precise straight lines is what allows the creation of more complex 3D architectures.

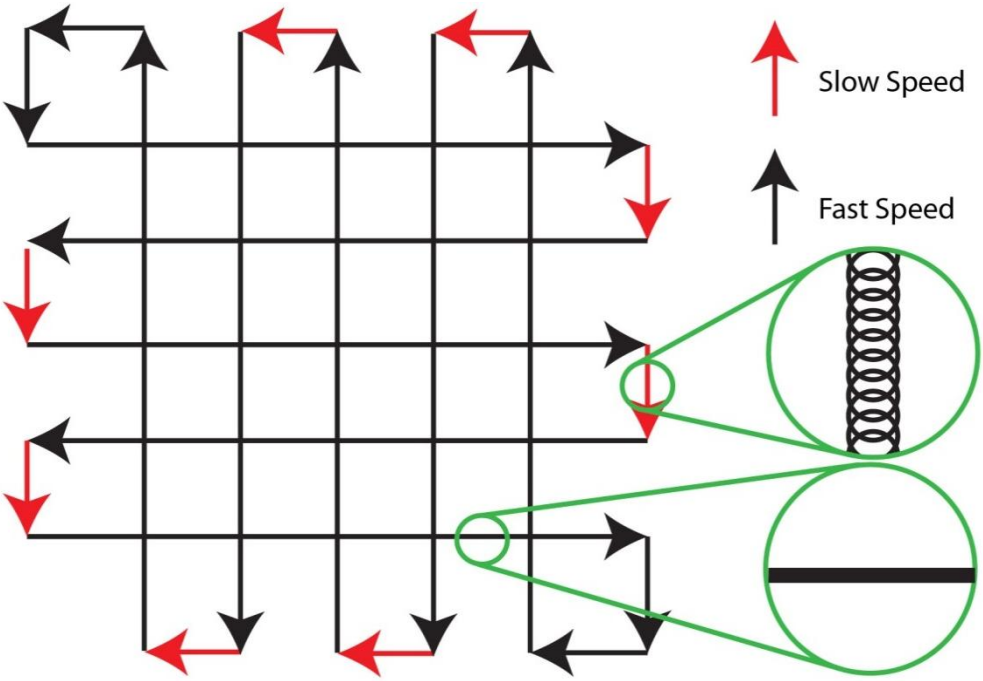

Figure S13. Design strategy for fabrication of fiber scaffold structures. A schematic diagram which illustrates the strategy used in designing fiber scaffolds. Straight line segments which compose the scaffold area are written using a 'fast speed'. When the collection electrode reaches a change in direction a 'slow speed' is used to allow the fiber jet to catch up with the stage movements, resulting in a coiled fiber segment. Combinations of fast and slow fiber segments lead to organized scaffolding structures.

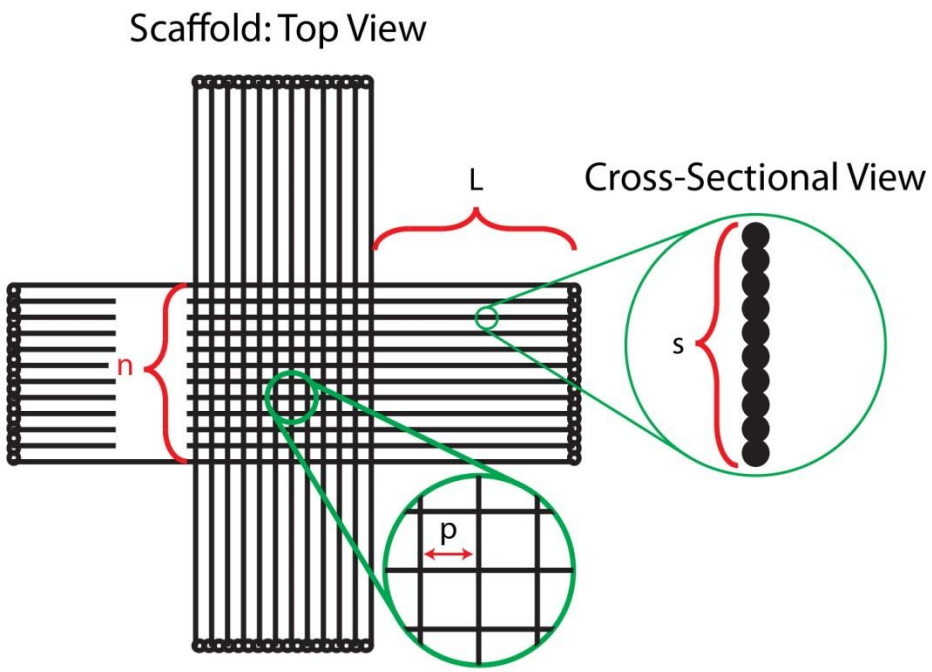

Figure S14. Design parameters for fabrication of fiber scaffold structures. A schematic diagram which illustrates the parameters used in designing fiber scaffolds with square pores. A square pore scaffold can have tunable pore size (p) which can be tessellated over the collection electrode to create n pores in either x or y dimension. A lead in length (L) is designed to enhance fiber deposition, and is optimized for the desired scaffold architecture. Repeating the scaffold pattern results in a honeycomb structured stacked fiber scaffold with s stacked fibers.

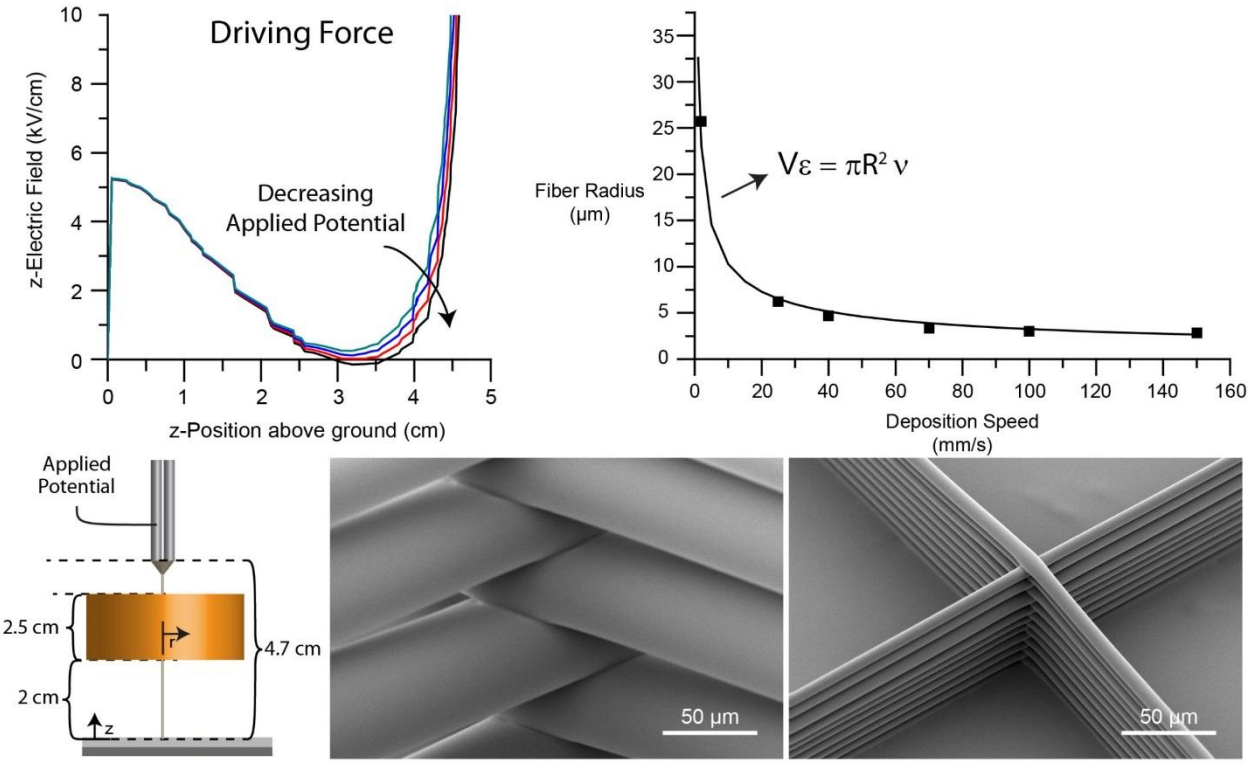

Figure S15. Controlling fiber diameter by adjusting fiber deposition speed through alteration of the z-electric field. PLGA fibers 50 μm in diameter were obtained by slowing down the depositing fiber jet to a speed of 2 mm/s. This was achieved through modulation of the electric field via the applied electric potential to the needle and secondary ring electrode. Using a similar technique, fibers with a diameter of 6 μm were achieved by increasing the fiber deposition speed to 100 mm/s. Comparing the theoretical fiber diameter calculated from the mass balance (solid line) to the fiber diameters measured experimentally (data points). The data points match closely to the predicted values, with error bars of measured fiber diameters being smaller than the data points on the plot. Scale bars indicate 50 μm.

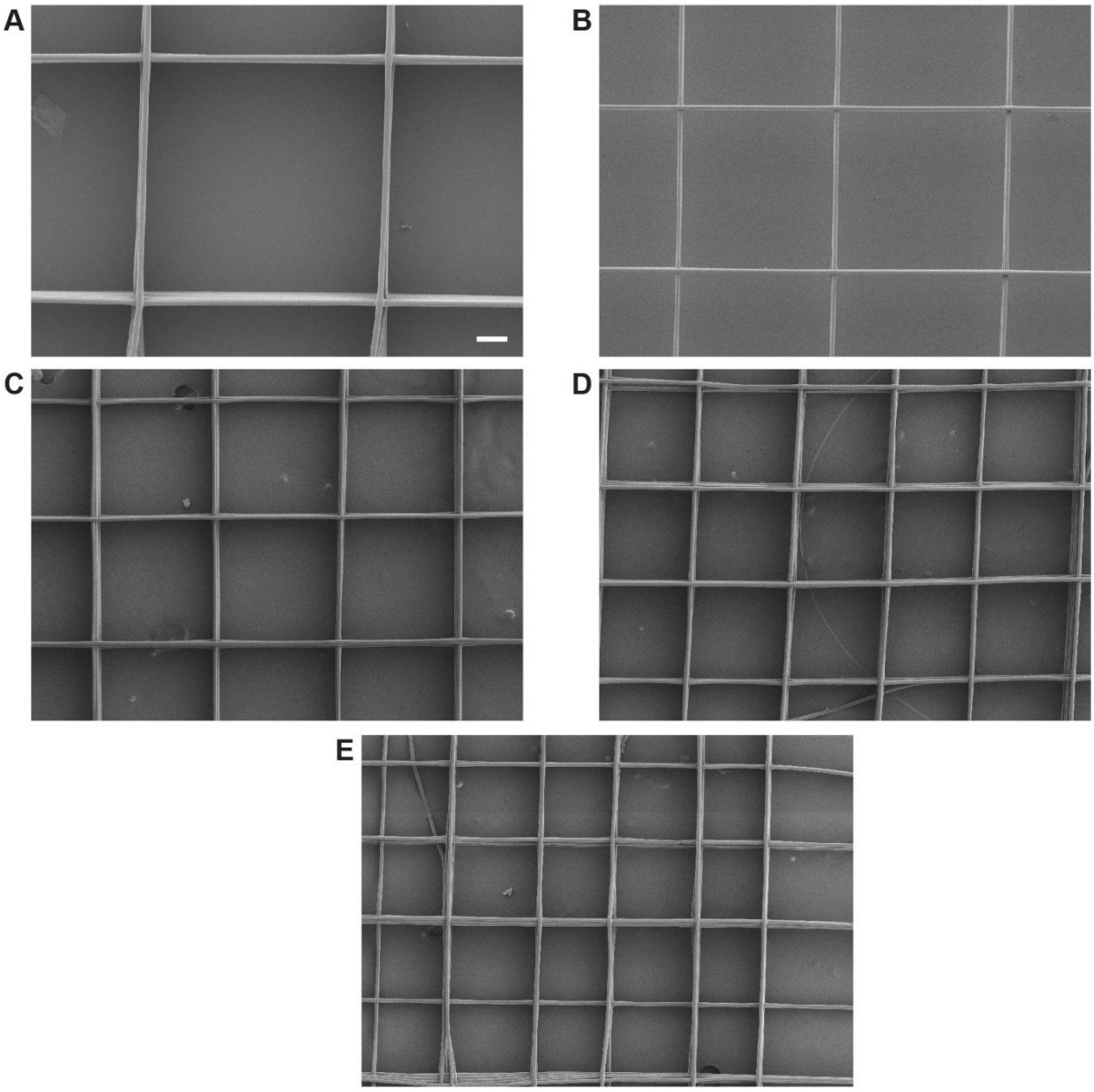

Figure S16. Controllable pore size scaffold from 3D jet writing. Scanning electron micrographs of scaffolds with the same pore shape, with differing pore size. These micrographs depict square honeycomb scaffold with pore sizes of 750 µm (A), 500 µm (B), 400 µm (C), 300 µm (D), and 250 µm (E). Each of the micrographs is at the same magnification, with the scale bar in (A) depicting 100 µm.

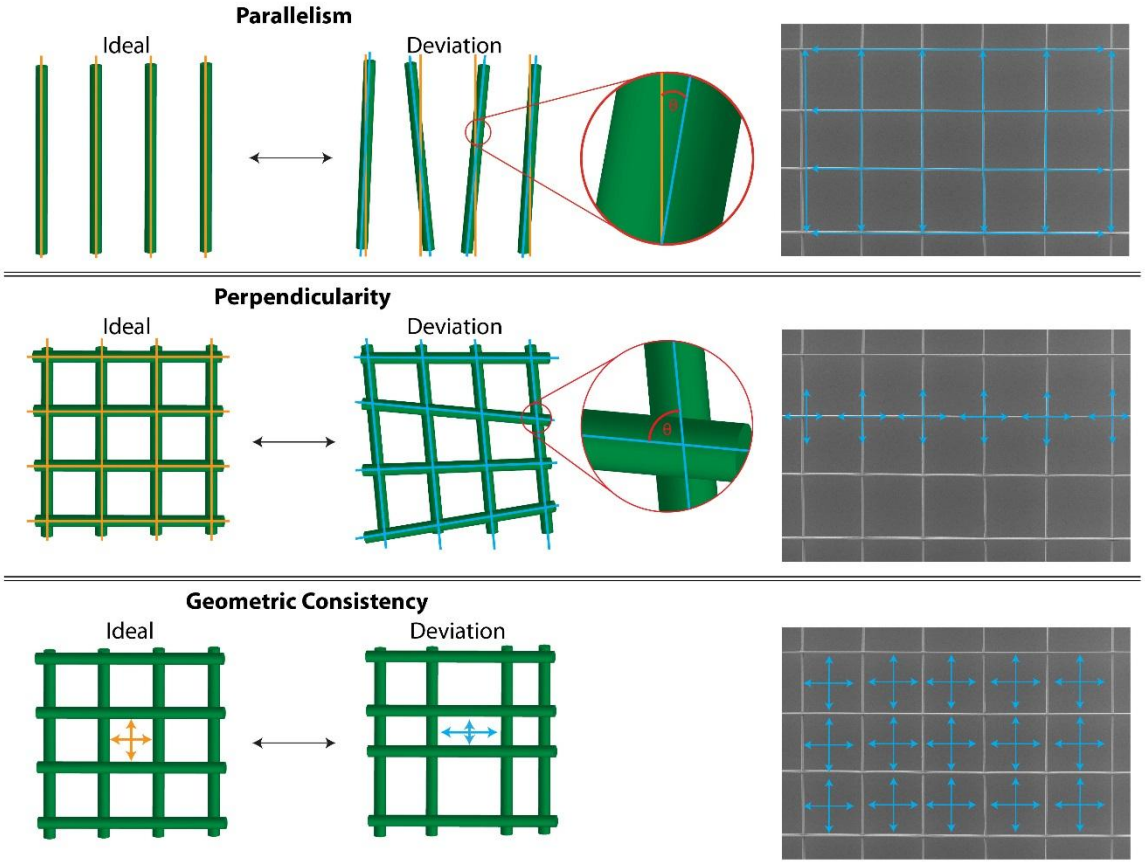

Figure S17. Example measurements used to determine fiber parallelism, perpendicularity, and geometric consistency. These three quantities were measured across three entire scaffolds using ImageJ analysis. Parallelism was used to describe how parallel fibers were relative to fibers running in the same direction. Perpendicularity describes how fibers running in opposite directions are oriented relative to one another. Geometric consistency is used as a measure of the regularity in the pore architectures achieved across the three scaffolds analyzed. On the SEM micrographs are examples of measurements taken in for each parameter.

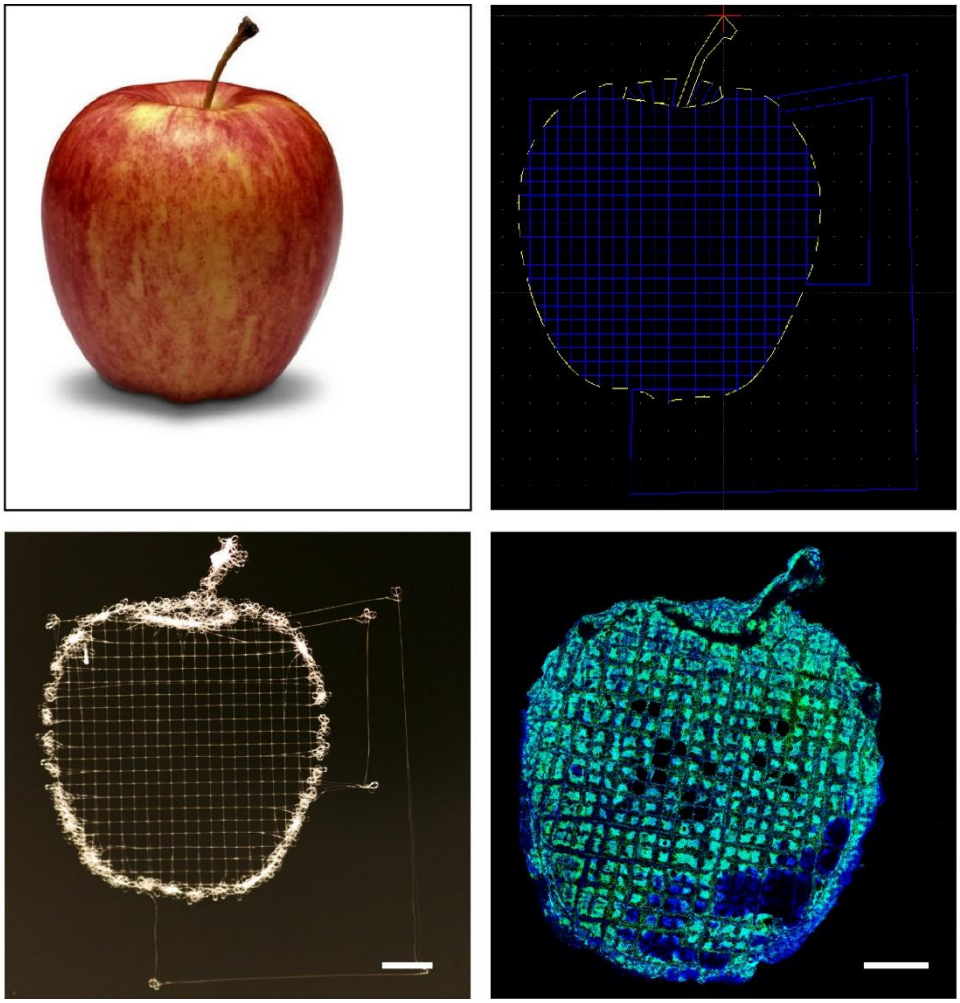

Figure S18. Digital images can be converted into 3D scaffolds which define areas for cell growth. Conversion of the figure of the apple to a CAD drawing enables fabrication of user defined scaffold geometries. Utilizing these scaffolds as 3D cell culture environments leads to customized cell growth areas.

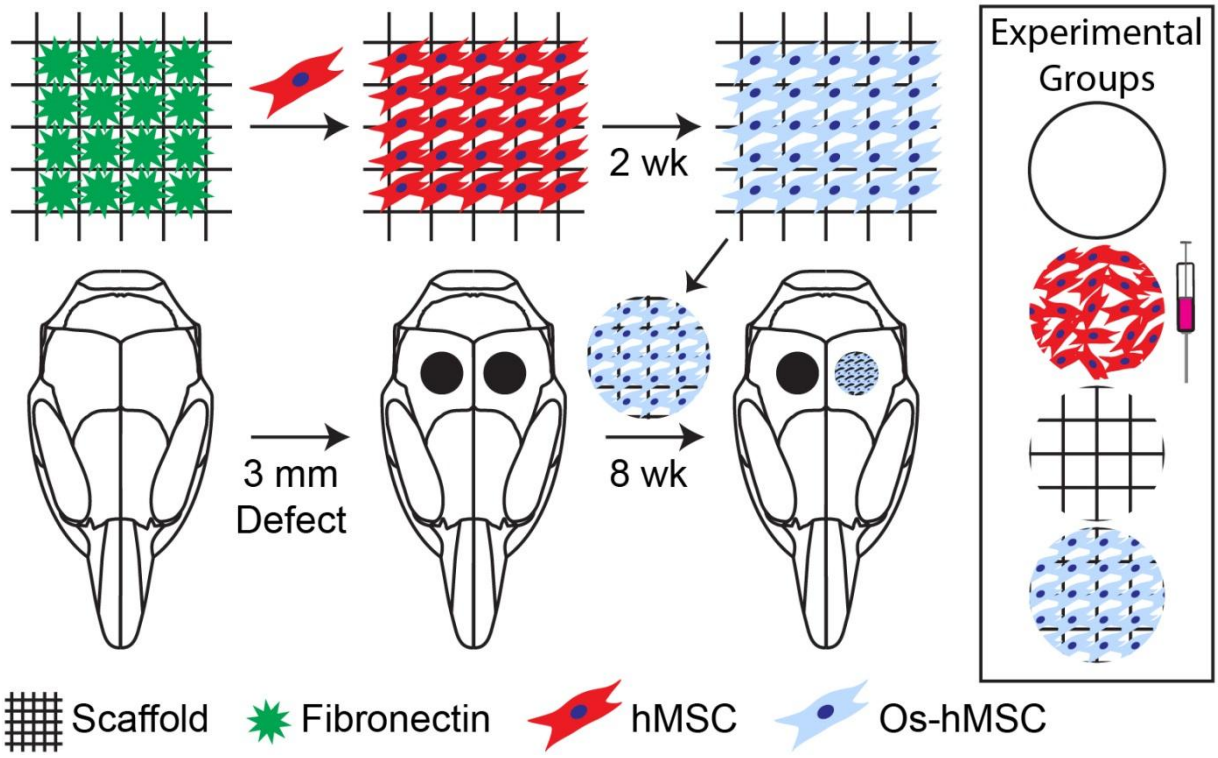

Figure S19. Schematic illustration of the calvarial defect model for tissue regeneration. Fibronectin coated scaffolds were incubated with hMSCs until confluence was reached. The stem cells were subsequently differentiated for two weeks using osteogenic differentiation medium. Two 3 mm defects were placed in the left and right parietal bone of the mouse, allowing for two groups to be tested in each mouse. Experimental groups included: No treatment, injection of hMSCs, scaffold implantation, and Os-hMSCs cultured on scaffolds. Circular cutouts of these scaffolds, equivalent injection of cells, or no treatment was administered directly to each defect site.

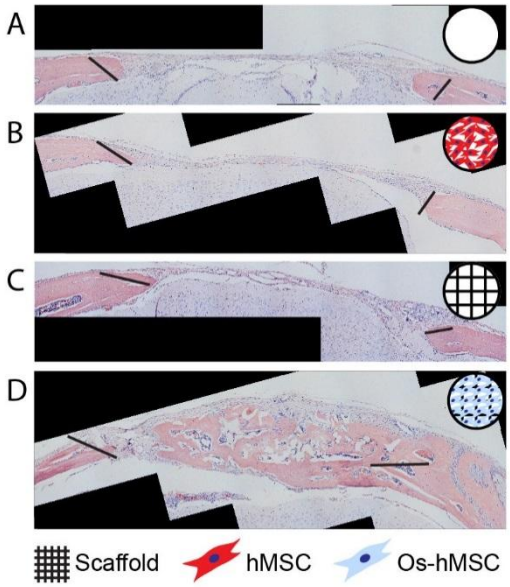

Figure S20. Full histological images of the defect sites. These images show that no treatment (A), hMSC injection (B), and scaffold only (C) treatment groups show little to no new bone growth across the entire defect site. These treatments only result in little bone ingrowth around the defect edge. Treatment using osteogenically differentiated hMSCs on scaffold (D) resulted in significant new bone volume within the defect, and nearly spans the entire defect site. Black lines delineate the original defect site as a reference to show the new bone volume.

Table S1. A summary of the precision at which the fibers can be deposited in a straight line is presented here. A 4x improvement was seen in straightness when a secondary ring electrode is present.

Measure	With Ring [pixels]	With Ring [µm]	Without Ring [pixels]	Without Ring [µm]
Average RMSE	0.57 ± 0.26	15 ± 6	2.29 ± 0.65	67 ± 23

Table S2. List of primers used for qPCR

Gene	UniGene	Amplicon Length
GAPDH	Hs.544577	93
ALPL	Hs.75431	79
SP7	Hs.209402	104
IBSP	Hs.518726	95

Movie S1. **A lag in deposition is required to deposit straight fiber segments.** Elimination of the liquid-rope coiling can be seen when the stage moves at a speed greater than the fiber deposition rate. Repeating the stage movements results in stacks of polymer fibers.